PHYSICAL REVIEW A **107**, 013107 (2023)

Photoelectron circular dichroism in fenchone by short coherent broadband laser pulses

Eric Kutscher, Anton N. Artemyev, and Philipp V. Demekhin*
Institut für Physik und CINSaT, Universität Kassel, Heinrich-Plett-Str. 40, 34132 Kassel, Germany

(Received 13 October 2022; accepted 15 December 2022; published 17 January 2023)

Photoelectron circular dichroism (PECD) of fenchone induced by short coherent broadband laser pulses is studied theoretically using the time-dependent single-center method. In particular, we investigate the chiral response to circularly polarized pulses with a sine-squared energy spectrum between 1 and 3 eV. We consider nonchirped and differently chirped pulses of a moderate peak intensity of 3×10^{12} W/cm^2 and a nonchirped pulse of a higher peak intensity of 1×10^{14} W/cm^2 leading to a strong-field ionization. Thereby, effects of the frequency ordering and pulse intensity are investigated in some detail. The present theoretical study predicts a substantial multiphoton PECD of fenchone, which can be manipulated by tailoring a spectral phase and intensity profile of a single coherent broadband laser pulse.

DOI: 10.1103/PhysRevA.107.013107

I. INTRODUCTION

When randomly oriented chiral molecules are ionized by circularly polarized light, photoelectrons are emitted with unequal probability in the forward versus backward directions with respect to the propagation direction of the light [1]. This fascinating chiroptical phenomenon, known as photoelectron circular dichroism (PECD), has been studied widely [2–5] since its first observation at the beginning of this century [6]. Because the effect arises already within the electric dipole approximation [1], the observed asymmetries are typically orders of magnitude larger than conventional circular dichroism in the absorption spectra. This enables chiral recognition in the gas phase by using circularly polarized light with sufficiently high photon energy at, e.g., large-scale synchrotron radiation facilities. In 2012 [7], table-top experiments with femtosecond laser pulses demonstrated that this effect persists also in the multiphoton ionization regime. Thereafter, PECD was investigated in many laser-driven regimes, e.g., in resonance-enhanced multiphoton ionization [7–12], above-threshold ionization [13–15], strong-field tunnel ionization [14–16], or two-color bichromatic [17,18] and pump-probe [19–21] regimes.

The one-photon PECD is known to depend on the radiation wavelength [22–24], since photoelectrons of different kinetic energies are released by different photon energies. In the multiphoton ionization regime, this dependence is by far nontrivial, since, in addition, different intermediate electronic states are involved in the multiphoton ionization path [25–28]. This opens a possibility for a coherent control [29,30] of the interference between different multicolor ionization pathways and, similarly to a control of other nonlinear chiroptical effects [31–33], of the multiphoton PECD [34]. Tailoring femtosecond laser pulses with octave-spanning spectral widths [35–38], which carry photons in a broad energy range, is a perspective route to achieve a control over the multiphoton PECD in chiral molecules. Here, not only a size of the PECD can be optimized [34] in order to increase precision of an enantiomeric excess determination, but also its emission-angle structuring or even its sign can be manipulated. In our previous theoretical work [39], we considered coherent broadband ionization of fenchone and found a substantial multiphoton PECD of its highest occupied molecular orbital (HOMO) on the order of 10%. In particular, we employed a short coherent pulse of a moderate peak intensity with the sine-squared energy spectrum in the range of 1–3 eV and considered a situation where photons of all energies are available at once (i.e., weak nonchirped pulse).

In the present work, we investigate a possibility of manipulating the multiphoton PECD of fenchone by tailoring a spectral phase and intensity of such coherent broadband pulses. This is proven to be a powerful way of a coherent control of the multiphoton ionization in atoms [40,41] and molecules [42,43]. For this purpose, we employ the time-dependent single-center (TDSC, [44]) method, which was successfully tested in our previous works [28,39] on the multiphoton ionization of fenchone in different regimes, and use short coherent broadband pulses with the same energy spectrum as in Ref. [39]. The paper is organized as follows. In Sec. II A we provide a brief description of the broadband pulses employed, while computational details are outlined in Sec. II B. In Sec. III A we investigate an effect of the ordering of frequencies in time, where photoionization proceeds temporarily via different intermediate electronic states. Thereafter, in Sec. III B we study the effect of the peak intensity and enter the strong-field ionization regime. We conclude in Sec. IV with a brief summary and outlook.

---

*demekhin@physik.uni-kassel.de

II. THEORY

The present calculations were performed using the TDSC method, which was introduced in detail in Ref. [44] and applied there to study photoionization and above-threshold ionization of a model chiral system. In the subsequent work [28], the method was adapted to study resonance-enhanced multiphoton ionization and above-threshold ionization of fenchone and camphor. In the recent work [39], multiphoton ionization of fenchone in different regimes, including strong-field, coherent broadband, and $\omega - 2\omega$ bichromatic ones was considered. The method consists of solving the three-dimensional time-dependent Schrödinger equation (TDSE) for a single active electron driven by arbitrary laser pulses in a molecular potential. We employ the dipole-velocity gauge for the light-matter interaction, since it improves convergence of the numerical solution of the TDSE over partial waves [45,46].

A. Broadband pulses

The normalized intensity spectrum of the presently considered broadband pulses is given by

$$I(\omega) = \sin^2\left(\pi \frac{\omega - \omega_1}{\omega_2 - \omega_1}\right), \quad \omega \in [\omega_1, \omega_2], \tag{1}$$

where, similarly to our previous study [39], we choose $\omega_1 = 1$ eV and $\omega_2 = 3$ eV. There the time envelope of the electric field of the pulse, $g_{\mathcal{E}}(t)$, was derived analytically for a nonchirped pulse by fixing the spectral phase function to a constant. The calculations in Ref. [39] were also performed in the velocity gauge, where, for simplicity, we used the same analytically derived time envelope of the pulse for the vector potential, i.e., we set $g_{\mathcal{A}}(t) = g_{\mathcal{E}}(t)$. This introduced a slight asymmetry of the intensity spectrum $I(\omega)$ with respect to the central (carrier) frequency $\omega_0 = (\omega_1 + \omega_2)/2$, and the resulting spectrum was slightly different from that given by Eq. (1) (see lower panel of Fig. 3 in Ref. [39]).

In the present study, we take a more rigorous route to construct the vector potential $\vec{A}(t)$ of laser pulses with the intensity spectrum $I(\omega)$ given by Eq. (1) and an arbitrary spectral phase function $\phi(\omega)$. For this purpose, we define the spectral function of the electric field via

$$\mathcal{E}(\omega) = \sqrt{I(\omega)}\, e^{-i\phi(\omega)}. \tag{2}$$

Hereafter, we Taylor expand the spectral phase function with respect to the central frequency ω_0:

$$\phi(\omega) = \phi_0 + \phi_1(\omega - \omega_0) + \frac{\phi_2}{2}(\omega - \omega_0)^2 + O(\omega^3). \tag{3}$$

The expansion coefficients ϕ_0, ϕ_1, and ϕ_2 represent, respectively, the carrier-envelope phase (CEP), a constant time shift, and an ordering of the frequencies (chirp) with a symmetric broadening in time [47]. More specifically, the frequencies are increasing in time from ω_1 to ω_2, if the chirp parameter $\phi_2 > 0$ (up-chirped pulse), and decreasing from ω_2 to ω_1 if $\phi_2 < 0$ (down-chirped pulse).

As was proposed in our previous work [39], we consider also here a random CEP of the pulse, which is anyway rather difficult to control for such pulses. Because we employ circularly polarized fields, a factor $e^{-i\phi_0}$ in Eq. (2) results in a rotation of the pulse around the laboratory z axis, which is given by the direction of the propagation of the pulse. The averaging over ϕ_0 recovers the axial symmetry of the pulse and thus of the resulting photoemission spectrum of randomly oriented molecules. It formally coincides with an integration over the azimuthal photoelectron emission angle φ. This integration can be performed analytically, while averaging over the molecular orientation Euler angle γ, which defines rotation around the laboratory z axis, needs to be performed numerically (see also discussion in Ref. [39] for more details). Without loss of generality, we thus chose $\phi_0 = 0$. We also set $\phi_1 = 0$, because an arbitrary time shift can later be applied to the vector potential $\vec{A}(t)$ by setting $t \to t - t_0$. Finally, we choose for the present study the chirp parameters $\phi_2 = 0$ fs^2 and ± 2 fs^2. Thereby, the chirped pulses with $\phi_2 = \pm 2$ fs^2 have very similar duration as compared to the nonchirped one with $\phi_2 = 0$ fs^2.

The time-dependent electric field is given by the inverse Fourier transformation of the spectral function (2):

$$\mathcal{E}(t) = \frac{1}{2\pi} \int_{\omega_1}^{\omega_2} \mathcal{E}(\omega) e^{i\omega t}\, d\omega. \tag{4}$$

This integration was performed numerically for the chosen chirp parameters ϕ_2 in the time interval of -15 fs $\leqslant t \leqslant 15$ fs. With the help of the complex field $\mathcal{E}(t)$, we now define the electric field vector of the circularly polarized pulse:

$$\vec{E}(t) = \mp E_0\{\mathrm{Re}[\mathcal{E}(t)], \pm \mathrm{Im}[\mathcal{E}(t)], 0\}, \tag{5}$$

where choosing "+" or "−" for its y component results in a positive or negative helicity of the field. The strength E_0 of the electric field (5) is defined (in atomic units) by the peak intensity of the pulse I_0 (which is given in units of W/cm^2) via $E_0 = \sqrt{\frac{I_0}{3.50945\times 10^{16}}}$. Finally, the vector potential of the pulse was numerically reconstructed via the integration

$$\vec{A}(t) = -\int_{-\infty}^{t} \vec{E}(t')\, dt', \tag{6}$$

and the pulse maximum was set to $t_0 = 15$ fs. The described procedure can straightforwardly be applied for any experimental energy spectrum $I(\omega)$ and chirp parameter ϕ_2.

Vector potentials of the circularly polarized up-, non-, and down-chirped pulses of a positive helicity, constructed as described above for the peak intensity of 3×10^{12} W/cm^2 considered here, are shown in the upper panel of Fig. 1 together with the respective projections $A_x(t)$ and $A_y(t)$. For a better representation, the up- and down-chirped pulses are shifted by the constant $\pm(0.25, 0.25, 0)$ a.u. with respect to the nonchirped pulse (positive shift for the up- and negative for the down-chirped pulse). A clear frequency ordering in time, from lower to higher ones (blue curves) and vice versa (red curves), as compared to the nonchirped pulse (black curves), can be seen from the upper panel of Fig. 1. From the lower panel of this figure, a symmetric broadening of the chirped pulses, introduced by the employed chirp parameters, can clearly be seen in the respective normalized intensities of the pulses $I(t)$. In particular, chirped pulses exhibit 15% larger full width durations at their half maxima, as compared to the nonchirped pulse.

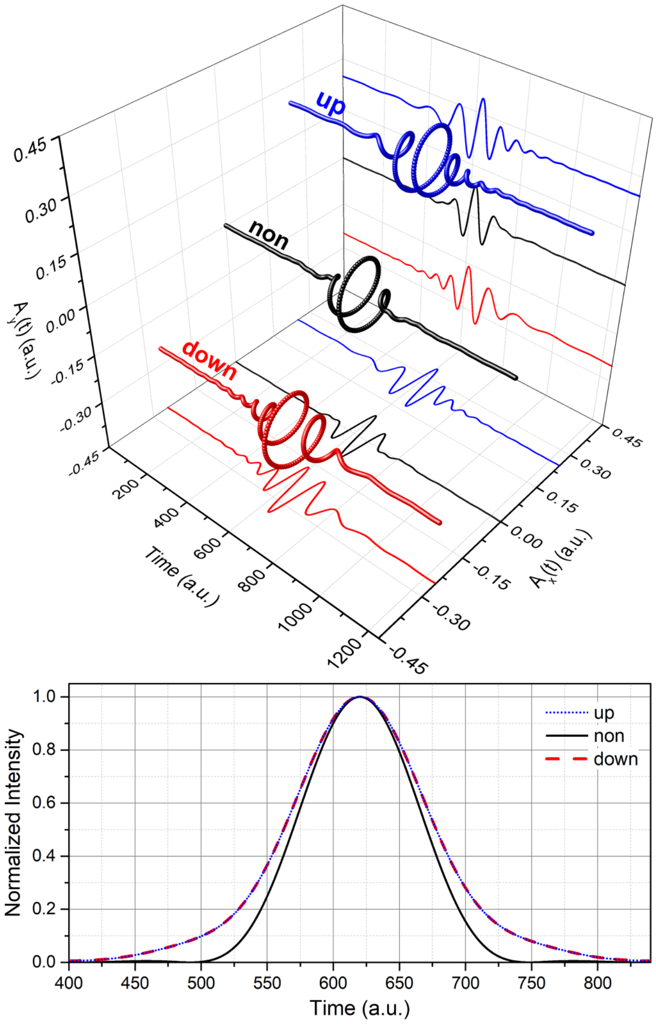

FIG. 1. Upper panel: Vector potentials $\vec{A}(t)$ and their x and y components of the considered up-chirped (uppermost blue trajectory and projections), nonchirped (middle black trajectory and projections), and down-chirped (lowermost red trajectory and projections) broadband laser pulses with respective chirp parameters $\phi_2 = +2, 0, -2$ fs^2. For a better comparison, the up- and down-chirped vector potentials are diagonally shifted by a constant. Lower panel: The respective normalized time envelopes of the field intensity $I(t)$. The parameters $\phi_2 = \pm 2$ fs^2 introduce a slight symmetrical broadening to the chirped pulses, which have very similar full widths at the half maximum than the nonchirped pulse (see legend).

B. Computational details

General computational details of the TDSC method can be found in Ref. [44], and that for fenchone in our previous works [28,39]. Therefore, only essential points are outlined below. For all calculations considering pulses with the peak intensity of 3×10^{12} W/cm^2, the radial grid was confined by $R_{\max} = 800$ a.u., while a larger grid with $R_{\max} = 1200$ a.u. was used for calculations considering the strong-field pulse of 1×10^{14} W/cm^2. The radial grid was divided into finite elements of different sizes in the inner and outer regions [28], each supporting normalized Lagrange interpolating polynomials constructed over 10 Gauss-Lobatto points [48–52]. The analytical expressions of all matrix elements are given in those works. As in our previous works on fenchone [28,39], we included partial photoelectron waves with the angular momenta and their projections limited by $\ell, |m| < 25$.

In order to account for the temporal structures of the pulses in Fig. 1, we chose a reasonable propagation time $T = 30$ fs $=$ 1240.24 a.u. for all calculations. The time-dependent electron wave packets were propagated using the short-iterative Lanczos method [53]. To save computation time, we used an earlier introduced "running grid" [54]. Here, we chose a linearly increasing grid size $R(t) = R_{\rm ini} + \frac{(R_{\max} - R_{\rm ini})}{T}\, t$ with $R_{\rm ini} = 25$ a.u. being the size of the box in which the initial state was found. By comparing two runs, performed with and without using the running grid, the convergence of the obtained results has been ensured. Employing this, reduced the computational time of each run by about 40%.

Calculations were performed for selected orientations of the molecule with respect to the laboratory frame. For this purpose, the initial electronic state and molecular potential were transformed to the laboratory frame. For each run, the final momentum distributions of the photoelectrons were obtained by a projection of the spatial wave packet onto Coulomb waves [39], which yields more accurate electron spectra than plane waves [28]. In order to exclude contributions to the photoelectron spectrum from highly excited bound states, the inner region of $R_{ion} < 60$ a.u. was excluded from the projection. Finally, the averaging over the molecular orientations Euler angles α, β, γ was performed numerically in steps of $\Delta\alpha = 0.2\pi$, $\Delta\beta = 0.1\pi$, and $\Delta\gamma = 0.5\pi$, which were found to ensure its convergence.

III. RESULTS AND DISCUSSION

The broadband laser pulses with the energy spectrum (1) imply multiphoton ionization of fenchone by the absorption of 3 to 9 photons (the binding energy of its HOMO is 8.6 eV [55]), involving thereby different intermediate electronic states in each photoabsorption step. The respective transition amplitudes of an infinite number of possible multiphoton ionization pathways superimpose coherently. In the nonchirped broadband pulse considered in our previous work [39], all photon energies supported by the pulse were available at once. Here, ordering of the frequencies in time will govern photoionization which proceeds temporarily via different intermediate electronic states. For the present study of the frequency ordering in Sec. III A, we use a moderate peak intensity of the pulse $I_0 = 3 \times 10^{12}$ W/cm^2 for up-, non-, and down-chirped pulses.

Increasing the pulse intensity influences transition probabilities in each photoabsorption step differently, changing thereby the relative contribution of each photoionization pathway in the total amplitude. For our study of this effect in Sec. III B, we use a nonchirped pulse with a stronger peak intensity $I_0 = 1 \times 10^{14}$ W/cm^2. Such photoionization cannot be quantified by a single Keldysh parameter [56], as in the case of monochromatic pulses. For the dominant central frequency of the pulse $\omega_0 = 2$ eV, the Keldysh parameter is equal to $\gamma \approx 1.1$. This indicates that ionization by the chosen pulse proceeds in an intermediate regime between the multiphoton ($\gamma \gg 1$) and strong-field tunnel ($\gamma \ll 1$) ionization.

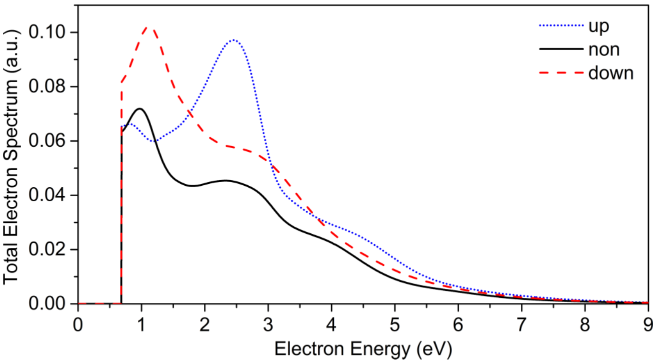

FIG. 2. Total photoelectron spectra as functions of the photoelectron kinetic energy ε computed for coherent broadband ionization of randomly oriented R(−) fenchone molecules with up-chirped (dotted blue curve), nonchirped (solid black curve), and down-chirped (dashed red curve) laser pulses of a moderate peak intensity $I_0 = 3 \times 10^{12}$ W/cm^2. Note that for the chosen propagation time, the slow photoelectrons with kinetic energies below 0.7 eV cannot be separated from the highly excited bound electronic states.

Finally, we remind that the considered here nonchirped pulse differs only slightly in its energy spectrum from that used in our previous work [39] (see discussion in the beginning of Sec. II A). As a consequence, the present results obtained for the nonchirped broadband pulse of the moderate intensity in Sec. III A are very similar to those obtained previously (see Fig. 4 in Ref. [39]). A tiny difference between those signals can be attributed to the difference in energy spectra of the pulses and a somewhat longer propagation performed in Ref. [39] on the falling edge of the pulse.

A. Frequency ordering

The total photoelectron spectra for the broadband ionization of fenchone with the up-, non-, and down-chirped pulses of moderate intensity are depicted in Fig. 2 (see legend). For the chosen total propagation times of 30 fs, the slow photoelectrons with the kinetic energies below 0.7 eV overlap with the highly excited bound electronic states. The respective contributions cannot be reliably extracted from the final photoelectron wave packet and are thus not shown in the figure. First of all, one can see that the integral signal (total number of photoelectrons) is noticeably larger for the somewhat longer chirped pulses (broken curves) as compared to the nonchirped pulse (solid curve). This is because using the same peak intensity for all pulses results in about 25% larger integral pulse intensity $\int I(t)\,dt$ for the former pulses as compared to the latter (see lower panel of Fig. 3).

As one also can see from Fig. 2, the spectrum computed for the nonchirped pulse (solid black curve) exhibits three maxima of an almost constant energy separation of about 1.5 eV. This indicates that the photoionization proceeds in the multiphoton regime with more photons being absorbed in the frequency range around 1.5 eV. The resulting spectrum thus represents an overlap of the broad photoionization and two decreasing in their intensity above-threshold ionization photoelectron peaks. Therefore, further above-threshold ionization with more absorbed photons is substantially suppressed, and

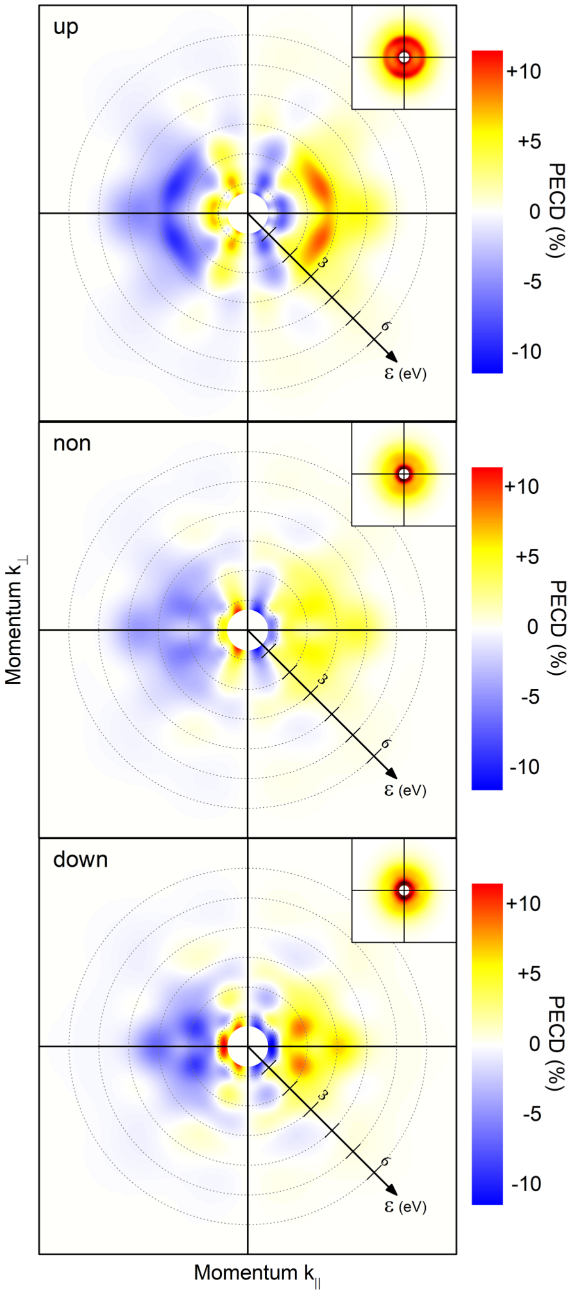

FIG. 3. Multiphoton PECD computed for coherent broadband ionization of randomly oriented R(−) fenchone molecules with up-chirped (upper panel), nonchirped (middle panel), and down-chirped (lower panel) laser pulses of a moderate peak intensity $I_0 = 3 \times 10^{12}$ W/cm^2 with the chirp parameters $\phi_2 = +2$, 0, and -2 fs^2, respectively. Shown is the relative difference between the two spectra obtained for circularly polarized pulses with the positive and negative helicities in percent of the maximal pixel intensity in the spectrum obtained for one of the helicities. The pulse propagates along $k_{||}$ from the left to the right. Note that the photoelectron momentum k is set on the linear scale of the kinetic energy ε, as shown by the downward inclined arrow with dotted concentric circles. The respective photoelectron spectra, computed for circularly polarized pulses with the positive helicity, are depicted as the insets to each panel. The respective total photoelectron spectra can be found in Fig. 2 (see also its caption for details).

the resulting spectrum vanishes already around $\varepsilon \approx 9$ eV. From the temporal point of view, the ionization is most probable when the pulse amplitude is reaching its maximum, and, for all three pulses, frequencies around the central frequency ω_0 dominate at these times. As a consequence, the spectra computed for the chirped pulses (broken curves in Fig. 2) exhibit similar structures with, however, different relative intensities. The latter can be rationalized by different excitation dynamics evoked by the frequency ordering.

In particular, in the moderate field regime considered here, the resonant excitation pathways are enhanced. In this way, by absorption of additional photons from the pulse, the HOMO electron climbs mainly a stair of intermediate electronic states by bound-bound transitions and populates thereby a dense spectrum of highly excited Rydberg states just below the photoionization threshold. Absorption of a subsequent photon from the pulse releases a photoelectron from those bound states in the continuum, which is less probable than bound-bound transitions. For the up-chirped pulse, only photons with higher energy of around 3 eV are available in the later times, and they create an additional portion of photoelectrons with the energy of around 2.5 eV (dotted blue curve in Fig. 2). On the contrary, only photons with low energy of around 1 eV can be absorbed on the falling edge of the down-chirped pulse, which enhances the respective photoelectron spectrum around 1 eV (dashed red curve). Since photons with all energies are available at the end of the nonchirped pulse and, among them, more photons are absorbed in the frequency range around 1.5 eV (see above), the first peak, according to this logic, appears in the spectrum of the nonchirped pulse around the photoelectron energies of 1 eV. Similar excitation dynamics were reported for the photoionization of atoms with chirped pulses [57,58]. A quantitative analysis of the temporal evolution of populations of intermediate electronic states is cumbersome, and it is outside the scope of the present work.

Figure 3 depicts multiphoton PECDs of fenchone computed for the coherent broadband ionization of its HOMO with the up- (upper panel), non- (middle panel), and down-chirped (lower panel) pulses. Each chiral asymmetry represents a difference between the two spectra, induced by the light with the positive and negative helicities (see below), and it is normalized to the maximal pixel intensity in the spectrum. It is shown in the momentum space $(k_\parallel, k_\perp)$, where the photoelectron emission angle is defined with respect to the light propagation direction from the left to the right along $k_\parallel$ (i.e., the left and right parts of the figure correspond to the backward and forward emission directions). For a better representation, the photoelectron momentum is set on the energy scale, as indicated by the downward incline arrows with dotted concentric circles. For clarity, the photoelectron spectra, computed for three circularly polarized pulses with the positive helicity, are depicted in the upper-right corners of each panel. These insets represent the same momentum space and energy scale as the main panels, and the photoelectron intensity is shown on the 0 to 1 scale by the white to black color palette. Note that, within the electric-dipole approximation used, interchanging of two enantiomers simply reverses sign of the PECD.

As one can see from this figure, all three pulses cause a substantial chiral asymmetry on the order of about 10% in a broad photoelectron energy range below about 6 eV. Dependencies of the computed PECD signals on the photoelectron energy and on the emission angle are however different for the three pulses. In particular, the signal computed for the nonchirped pulse (middle panel of Fig. 3) can roughly be divided in two regions. The inner region represents a sharply structured “butterfly” with a negative PECD, and the outer region exhibits a positive weakly structured PECD. Such a change of sign of the dichroism across the spectral maximum is analogous to the anomalous dispersion of the dichroic parameter across resonances [59,60]. For the up-chirped pulse (upper panel), the inner structure is stretched to higher photoelectron energies, and PECD in the outer region is significantly enhanced. Thereby, one expects negative PECD in a broader interval of the kinetic energies and a somewhat stronger positive PECD in the narrower, as compared to the nonchirped pulse. For the down-chirped pulse (lower panel), the inner structure is compressed to lower photoelectron energies, such that negative PECD can be observed only in a narrow kinetic energy range. In addition, strength of the positive PECD in the broad outer region is somewhat increased, as compared to the nonchirped pulse.

B. Strong field ionization

The two-dimensional photoelectron spectrum of fenchone, computed for the stronger nonchirped broadband pulse of a positive helicity, is shown in the upper panel of Fig. 4 in the momentum space, in the way similar to Fig. 3. This photoelectron signal is normalized to the maximal pixel intensity and, for the reasons explained in the preceding section, shown only for photoelectrons with the kinetic energies $\varepsilon > 1.7$ eV. As one can see, the photoelectrons are predominantly emitted along the polarization plane of the circularly polarized field (vertical direction), which is typical for the strong-field tunnel ionization. Although we show only a fraction of slower photoelectrons with kinetic energies below about 10 eV, where a larger chiral asymmetry can be expected, considerably more electrons are emitted with higher energies. This can be recognized from the inset to this panel, which depicts an overview of the total photoelectron spectrum. As one can see, the computed total spectrum falls almost exponentially and vanishes at kinetic energies of about 40 eV. Thus, the stronger pulse produces photoelectrons with almost four times larger kinetic energies as compared to the weaker pulse (compare with solid black curve in Fig. 2).

The respective PECD, obtained as described in the preceding section, is depicted in the lower panel of Fig. 4. Surprisingly, this signal looks as a stretched version of the PECD induced by the weaker nonchirped pulse (middle panel of Fig. 3). In particular, one recognizes a very similar inner region of a sharply structured “butterfly” form with a negative asymmetry. This region covers photoelectrons with almost four times larger kinetic energies, as compared to the weaker nonchirped pulse. The overall strength of the PECD, however, drops by almost four times below about 3%. The outer region in the lower panel of Fig. 4 exhibits also a weakly structured positive effect. However, its strength is considerably smaller than that for the weaker nonchirped pulse. This can be explained by the presently used normalization of the asymmetry to the spectrum’s maximum. For such exponentially falling

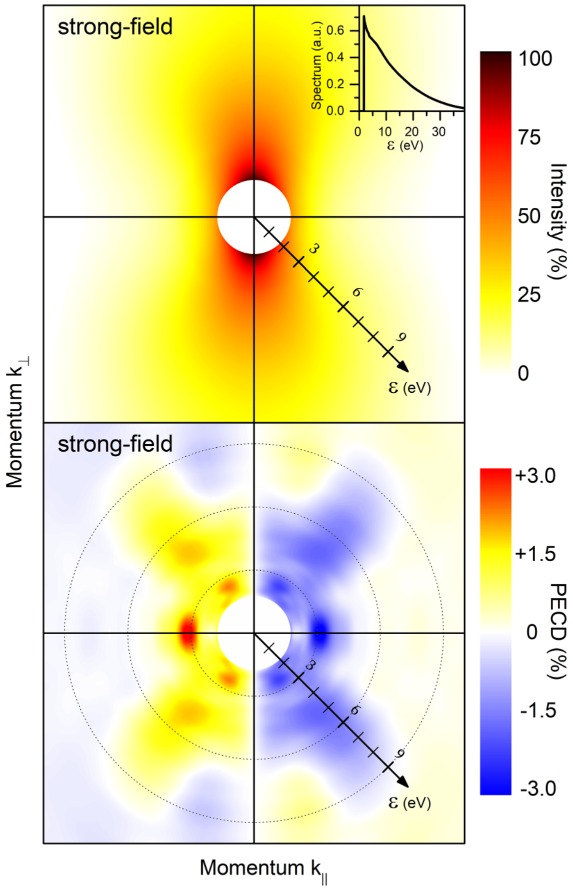

FIG. 4. Upper panel: The photoelectron spectrum computed for strong-field ionization of randomly oriented R(−) fenchone molecules excited by a circularly polarized coherent broadband pulse with a positive helicity and peak intensity $I_0 = 1 \times 10^{14}$ W/cm^2. Note that for the chosen propagation time, the slow photoelectrons with kinetic energies below 1.7 eV cannot be separated from the highly excited bound electronic states. The spectrum is normalized to the maximum pixel intensity and the photoelectron momentum is set on the linear scale of the kinetic energy ε, as is shown by the downward inclined arrow with dotted concentric circles. The inset depicts the respective total photoelectron spectrum. Lower panel: Corresponding multiphoton PECD shown in percent of the maximal pixel intensity of the spectrum from the upper panel (see caption of Fig. 3 for details on the data representation).

spectra, an energy-dependent normalization could be more suitable.

IV. CONCLUSIONS

The multiphoton PECD of randomly oriented R(−) fenchone molecules is studied theoretically with the time-dependent single-center method in the coherent broadband ionization regime by considering differently chirped laser pulses supporting photons with energies from 1 eV to 3 eV. The chirp parameters $\phi_2 = \pm 2$ fs^2 are chosen to keep the total pulse durations very similar to that of the nonchirped pulse with $\phi_2 = 0$ fs^2, and the peak intensities 3×10^{12} and 1×10^{14} W/cm^2 to stay in the weak-field multiphoton and strong-field ionization regimes, respectively. The present results obtained for the weaker nonchirped pulse are in agreement with that from our previous study [39], suggesting that slight modifications of the spectrum of nonchirped broadband pulses cause minor changes in the resulting PECD.

On the other hand, a considerable stretching to higher or compression to lower kinetic energies of the computed PECD signal is found for the up- or down-chirped pulses of the weaker peak intensity, respectively, as compared to the nonchirped pulse. This can be attributed to different photoionization dynamics governed by the frequency ordering, resulting in superposition of different multiphoton ionization pathways for different ϕ_2. Utilizing the nonchirped broadband pulse of the stronger peak intensity introduces an almost four time stretching of the total spectrum and of the respective PECD signal to higher photoelectron kinetic energies, but the chiral asymmetry drops by a factor of about 4, as compared to the weaker pulse.

The present theoretical results illustrate that a single broadband pulse can be used as a perspective tool for the coherent control of PECD [34]. Introducing higher expansion terms in the spectral phase and variations of the intensity profile, as a future route to control PECD in a desirable way, are outside the scope of the present proof-of-principle theoretical study. The present conclusions are relevant for coherent control of other nonlinear chiroptical effects.

ACKNOWLEDGMENTS

We acknowledge T. Baumert for many valuable discussions. This work was funded by the Deutsche Forschungsgemeinschaft (DFG), Project No. 328961117 — SFB 1319 ELCH (Extreme light for sensing and driving molecular chirality, project C1).

---

[1] B. Ritchie, Phys. Rev. A **13**, 1411 (1976).
[2] I. Powis, Adv. Chem. Phys. **138**, 267 (2008).
[3] L. Nahon, G. A. Garcia, and I. Powis, J. Electron Spectrosc. Relat. Phenom. **204**, 322 (2015).
[4] S. Turchini, J. Phys.: Condens. Matter **29**, 503001 (2017).
[5] R. Hadidi, D. K. Bozanic, G. A. Garcia, and L. Nahon, Adv. Phys. X **3**, 1477530 (2018).
[6] N. Böwering, T. Lischke, B. Schmidtke, N. Müller, T. Khalil, and U. Heinzmann, Phys. Rev. Lett. **86**, 1187 (2001).
[7] C. Lux, M. Wollenhaupt, T. Bolze, Q. Liang, J. Köhler, C. Sarpe, and T. Baumert, Angew. Chem. Int. Ed. **51**, 5001 (2012).
[8] C. S. Lehmann, N. B. Ram, I. Powis, and M. H. M. Janssen, J. Chem. Phys. **139**, 234307 (2013).
[9] N. B. Ram, C. S. Lehmann, and M. H. M. Janssen, EPJ Web Conf. **41**, 02029 (2013).
[10] C. Lux, M. Wollenhaupt, C. Sarpe, and T. Baumert, Chem. Phys. Chem. **16**, 115 (2015).
[11] M. H. M. Janssen and I. Powis, Phys. Chem. Chem. Phys. **16**, 856 (2014).

[12] A. Kastner, T. Ring, H. Braun, A. Senftleben, and T. Baumert, Chem. Phys. Chem. **20**, 1416 (2019).

[13] C. Lux, A. Senftleben, C. Sarpe, M. Wollenhaupt, and T. Baumert, J. Phys. B **49**, 02LT01 (2016).

[14] S. Beaulieu, A. Ferré, R. Géneaux, R. Canonge, D. Descamps, B. Fabre, N. Fedorov, F. Légaré, S. Petit, T. Ruchon *et al.*, New J. Phys. **18**, 102002 (2016).

[15] S. Beaulieu, S. Comby, B. Fabre, D. Descamps, A. Ferré, G. Garcia, R. Géneaux, F. Légaré, L. Nahon, S. Petit *et al.*, Faraday Discuss. **194**, 325 (2016).

[16] R. Cireasa, A. E. Boguslavskiy, B. Pons, M. C. H. Wong, D. Descamps, S. Petit, H. Ruf, N. Thiré, A. Ferré, J. Suarez *et al.*, Nat. Phys. **11**, 654 (2015).

[17] Ph. V. Demekhin, A. N. Artemyev, A. Kastner, and T. Baumert, Phys. Rev. Lett. **121**, 253201 (2018).

[18] S. Rozen, A. Comby, E. Bloch, S. Beauvarlet, D. Descamps, B. Fabre, S. Petit, V. Blanchet, B. Pons, N. Dudovich, and Y. Mairesse, Phys. Rev. X **9**, 031004 (2019).

[19] A. Comby, S. Beaulieu, M. Boggio-Pasqua, D. Descamps, F. Légareé, L. Nahon, S. Petit, B. Pons, B. Fabre, Y. Mairesse, and V. Blanchet, J. Phys. Chem. Lett. **7**, 4514 (2016).

[20] S. Beaulieu, A. Comby, A. Clergerie, J. Caillat, D. Descamps, N. Dudovich, B. Fabre, R. Géneaux, F. Légaré, S. Petit *et al.*, Science **358**, 1288 (2017).

[21] S. Beaulieu, A. Comby, D. Descamps, B. Fabre, G. A. Garcia, R. Géneaux, A. G. Harvey, F. Légaré, Z. Mašín, L. Nahon *et al.*, Nat. Phys. **14**, 484 (2018).

[22] S. Turchini, N. Zema, G. Contini, G. Alberti, M. Alagia, S. Stranges, G. Fronzoni, M. Stener, P. Decleva, and T. Prosperi, Phys. Rev. A **70**, 014502 (2004).

[23] S. Stranges, S. Turchini, M. Alagia, G. Alberti, G. Contini, P. Decleva, G. Fronzoni, M. Stener, N. Zema, and T. Prosperi, J. Chem. Phys. **122**, 244303 (2005).

[24] G. A. Garcia, L. Nahon, S. Daly, and I. Powis, Nat. Commun. **4**, 2132 (2013).

[25] M. M. Rafiee Fanood, M. H. M. Janssen, and I. Powis, J. Chem. Phys. **145**, 124320 (2016).

[26] A. Kastner, T. Ring, B. C. Krüger, G. B. Park, T. Schäfer, A. Senftleben, and T. Baumert, J. Chem. Phys. **147**, 013926 (2017).

[27] R. E. Goetz, T. A. Isaev, B. Nikoobakht, R. Berger, and C. P. Koch, J. Chem. Phys. **146**, 024306 (2017).

[28] A. D. Müller, A. N. Artemyev, and Ph. V. Demekhin, J. Chem. Phys. **148**, 214307 (2018).

[29] M. Shapiro and P. Brumer, *Quantum Control of Molecular Processes* (Wiley-VCH, Berlin, 2011).

[30] M. Wollenhaupt and T. Baumert, Faraday Discuss. **153**, 9 (2011).

[31] P. Fischer and F. Hache, Chirality **17**, 421 (2005).

[32] D. Ayuso, A. F. Ordonez, and O. Smirnova, Phys. Chem. Chem. Phys. **24**, 26962 (2022).

[33] J. R. Rouxel and S. Mukamel, Chem. Rev. **122**, 16802 (2022).

[34] R. E. Goetz, C. P. Koch, and L. Greenman, Phys. Rev. Lett. **122**, 013204 (2019).

[35] D. Wildanger, E. Rittweger, L. Kastrup, and S. W. Hell, Opt. Express **16**, 9614 (2008).

[36] H. Hundertmark, S. Rammler, T. Wilken, R. Holzwarth, T. W. Hänsch, and P. St. J. Russell, Opt. Express **17**, 1919 (2009).

[37] S. Kerbstadt, D. Timmer, L. Englert, T. Bayer, and M. Wollenhaupt, Opt. Express **25**, 12518 (2017).

[38] S. Kerbstadt, D. Pengel, L. Englert, T. Bayer, and M. Wollenhaupt, Phys. Rev. A **97**, 063402 (2018).

[39] A. D. Müller, E. Kutscher, A. N. Artemyev, and Ph. V. Demekhin, J. Chem. Phys. **152**, 044302 (2020).

[40] M. Krug, T. Bayer, M. Wollenhaupt, C. Sarpe-Tudoran, T. Baumert, S. S. Ivanov, and N. V. Vitanov, New J. Phys. **11**, 105051 (2009).

[41] D. Zille, D. Adolph, M. Möller, A. M. Sayler, and G. G. Paulus, New J. Phys. **20**, 063018 (2018).

[42] N. Reusch, S. Griebe, J. Karges, and K.-M. Weitzel, Z. Phys. Chem. **229**, 1729 (2015).

[43] B. Kaufman, T. Rozgonyi, P. Marquetand, and T. Weinacht, Phys. Rev. A **103**, 023108 (2021).

[44] A. N. Artemyev, A. D. Müller, D. Hochstuhl, and Ph. V. Demekhin, J. Chem. Phys. **142**, 244105 (2015).

[45] E. Cormier and P. Lambropoulos, J. Phys. B **29**, 1667 (1996).

[46] Y.-C. Han and L. B. Madsen, Phys. Rev. A **81**, 063430 (2010).

[47] M. Wollenhaupt, A. Assion, and T. Baumert, Short and ultrashort laser pulses, in *Springer Handbook of Lasers and Optics*, edited by F. Träger (Springer, Heidelberg, 2012), pp. 1047–1094.

[48] Ph. V. Demekhin, D. Hochstuhl, and L. S. Cederbaum, Phys. Rev. A **88**, 023422 (2013).

[49] A. N. Artemyev, A. D. Müller, D. Hochstuhl, L. S. Cederbaum, and Ph. V. Demekhin, Phys. Rev. A **93**, 043418 (2016).

[50] A. N. Artemyev, L. S. Cederbaum, and Ph. V. Demekhin, Phys. Rev. A **95**, 033402 (2017).

[51] A. N. Artemyev, L. S. Cederbaum, and Ph. V. Demekhin, Phys. Rev. A **96**, 033410 (2017).

[52] A. N. Artemyev, A. I. Streltsov, and Ph. V. Demekhin, Phys. Rev. Lett. **122**, 183201 (2019).

[53] T. J. Park and J. C. Light, J. Chem. Phys. **85**, 5870 (1986).

[54] E. Kutscher, A. N. Artemyev, and Ph. V. Demekhin, Front. Chem. **10**, 809137 (2022).

[55] I. Powis, C. J. Harding, G. A. Garcia, and L. Nahon, Chem. Phys. Chem. **9**, 475 (2008).

[56] L. V. Keldysh, Sov. Phys. JETP. **20**, 1307 (1965).

[57] T. Nakajima, Phys. Rev. A **75**, 053409 (2007).

[58] S. Laulan, J. Haché, H. S. Ba, and S. Barmaki, J. Mod. Phys. **04**, 20 (2013).

[59] D. Catone, M. Stener, P. Decleva, G. Contini, N. Zema, T. Prosperi, V. Feyer, K. C. Prince, and S. Turchini, Phys. Rev. Lett. **108**, 083001 (2012).

[60] G. Hartmann, M. Ilchen, Ph. Schmidt, C. Küstner-Wetekam, C. Ozga, F. Scholz, J. Buck, F. Trinter, J. Viefhaus, A. Ehresmann *et al.*, Phys. Rev. Lett. **123**, 043202 (2019).